

# DETC2022-XXXX

## EXPERIMENTAL INVESTIGATION OF TOPOLOGY-OPTIMIZED BEAMS WITH ISOTROPIC AND ANISOTROPIC BASE MATERIAL ASSUMPTIONS

**Hajin Kim**

Department of Civil and Environmental Engineering  
 Massachusetts Institute of Technology  
 Cambridge, MA

**Josephine V. Carstensen**

Department of Civil and Environmental Engineering  
 Massachusetts Institute of Technology  
 Cambridge, MA

### ABSTRACT

Additive Manufacturing (AM) technologies are promising fabrication methods with the potential to increase customizability and structural complexity. It is well established that the nature of AM typically results in base materials that exhibit an extent of anisotropy. Since topology optimization is a freeform approach that generally achieves high performing designs, it is often suggested as a powerful design-for-AM method. However, most topology optimization frameworks ignore anisotropic effects and assume isotropy of the base material. Although frameworks that consider anisotropy have been suggested, the influence anisotropy has on the physical behavior of fabricated designs is not well understood. Therefore, this work presents an experimental study of topology-optimized structures designed with both isotropic and anisotropic linear elastic material assumptions to explore how much anisotropic considerations matter when it comes to the discrepancy in numerical and experimental performance. The experimental investigation is conducted using a Fused Filament Fabrication print process that allows us to prescribe the anisotropy. The Young's Modulus of the designated print setup is experimentally determined and used for design of 3D simply supported beams with various material volumes. Samples are fabricated and evaluated using 3-point bending tests. It is seen that the isotropic designs have a slightly better average performance at the design load (1.8 – 2.0%), but that inclusion of the anisotropic behavior significantly limits behavioral differences across samples (84.4 – 171.5% decrease in standard deviation) and improves the print success rate.

Keywords: Topology Optimization, Anisotropy, Experimental, Fabrication, Additive Manufacturing

### NOMENCLATURE

$\mathbf{B}^e$	strain displacement matrix
$c$	constitutive matrix coefficient
$\mathbf{D}$	constitutive matrix
$\mathbf{d}$	nodal displacements
$d_1 \dots 5$	dog-bone specimen dimensions
$E$	Young's modulus
$e$	element
$\mathbf{F}$	global node vector
$f$	objective function
$G$	shear modulus
$g$	volume constraint
$H$	height of design domain
$h$	static equilibrium
$\mathbf{K}_e$	element stiffness matrix
$\mathbf{K}_0^e$	element stiffness matrix of pure solid material
$\mathbf{K}(\rho)$	global stiffness matrix
$L$	length of design domain
$P$	applied load
$r_{min}$	minimum length scale
$V$	desired volume
$v^e$	elemental volume
$W$	width of design domain
$\beta$	Heaviside parameter
$\Delta\eta$	stepsize/change in eta
$\eta$	SIMP penalty term
$\nu$	Poisson's ratio
$\rho^e$	densities of finite elements (design variable)
$\rho_{min}^e$	minimum allowable elemental density
$\Omega$	design domain

## 1. INTRODUCTION

A material that exhibits directionally dependent behavior is considered an anisotropic material. Anisotropy is seen in many common materials including timber, biological tissues, graphite, and numerous composites [1]. For the example of timber, anisotropy is evident when looking at the material properties along the grain versus across the grain. Timber is composed of long cellulose fibers that are aligned with the direction of growth of the tree and held together in a matrix of rigid lignin. These long fibers are much harder to pull apart than the stiff matrix that the fibers are suspended in, thus resulting in anisotropic material behavior. In contrast, a material is isotropic if it has the same behavior, regardless of its loading direction. Examples of isotropic materials include most hot rolled metals.

An anisotropic material behavior can be either innate to the material structure (as for timber) or induced via the fabrication method (e.g., fiber reinforcement of isotropic plastic). The recent rapid developments of Additive Manufacturing (AM) fabrication techniques have revolutionized fabrication [2]–[4] and unlocked increasingly complex manufacturing possibilities. ASTM defines AM as “the process of joining materials to make objects from 3D model data, usually layer upon layer” [5]. AM processes have been developed using various base material systems including metals, ceramics, polymers and composites. A detailed review of all AM processes is beyond the scope of the current paper, the reader is referred to [6]. Although varying significantly depending on the specific technology, it is well-documented that AM produced materials exhibit some extent of anisotropy [7]. The two primary causes for the anisotropic behavior are the so-called process induced anisotropy resulting from the layer-by-layer manufacturing process [8], and intrinsic anisotropy which is a result of design decision such as choice of lattice infill [9]. For some AM processes, the anisotropy can be observed in both the elastic modulus and yield properties [9], [10].

Although material anisotropy is well established phenomena, the effect it imposes on resulting designs is not well understood. This work will examine the effect on the physical specimen behavior of including anisotropy in a free form design algorithm. Herein we design, fabricate, test, and compare 3D structures with anisotropic base materials. Freeform designs are obtained with both isotropic and anisotropic assumptions. Since AM processes allow for simulations manufacture of both the local material and the structures, the designs herein are fabricated using the polymer-based AM process of Fused Filament Fabrication (FFF). This allows us to explicitly control the directionality of the base material behavior.

FFF is a material extrusion-based AM process which typically produces material anisotropy [11], [12]. Extrusion based fabrication techniques involves feeding material (referred to from here on out as filament) through a nozzle/extruder and depositing the filament layer-by-layer. Interfilament gaps often lead to weakened bonds and subsequently weakened behavior in the material [14], [15]. Anisotropic behaviors also arise when layers bond improperly. However, specimens printed using FFF exhibit anisotropic behavior not only due to the layer-wise

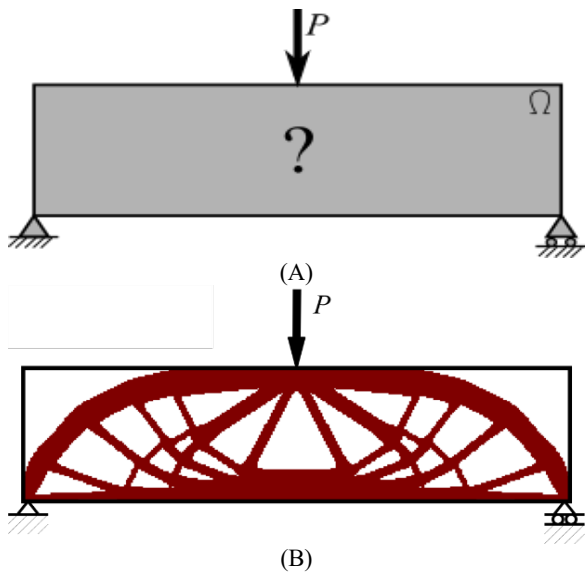


**FIGURE 1: ILLUSTRATION OF A 2D DESIGN DOMAIN FOR A SIMPLY SUPPORTED BEAM, AND (B) THE RESULTANT TOPOLOGY OPTIMIZED SOLUTION.**

manufacturing, but also because filament is used as its feedstock material [16].

Since topology optimization is often mentioned as a promising tool in design-for-AM [17], [18], this work will use topology optimization to generate all 3D structural designs. Topology optimization is a free-form design method that seeks to determine a material distribution within a given design domain with applied loads and boundary conditions. As shown in Fig. 1a, it does not require the user to have a preconceived notion of the final design layout. The results, as e.g. shown in Fig. 1b, are therefore often high performing and geometrically complex [18]. In topology optimization the design problem is posed as a formal optimization problem, and most rigorously solved using a mathematical program. There exist several approaches to topology optimization including density-based, level set and evolutionary methods [19]. Most commonly, regardless of the used approach, the design domain is discretized using finite elements. This allows for a computational evaluation of the design performance. However, the discretization essentially creates a binary optimization problem where the density  $\rho^*$  of the final elements should be either 0 or 1 to signal if it is efficient to place material at a given point in space. With the often high number of design variables involved (especially for 3D designs), the binary optimization problem is in most approaches relaxed such that  $0 \leq \rho^* \leq 1$  to allow the use of gradient-based optimizers [20]. In the density-based approach [21] which will be used herein, this is coupled with a penalization scheme that guides the design towards a 0-1 solution.

Most research on topology optimization assumes isotropic, linear elastic behavior of the base material. However, in efforts to tailor the design technology to fabrication by AM processes, there are currently many efforts to address anisotropy within topology optimization frameworks [22]. These mostly

focus on incorporating the toolpath or deposition path [23]–[27], and optimization of build direction (see e.g. [28], [29]). More recently, a strength-based topology optimization framework has been suggested using a Tsai-Wu failure criterion [30], [31]. However, there is a distinct lack in the literature on how important it is to factor in anisotropy when it comes to the final fabricated product of topology-optimized designs.

This work seeks to investigate the effects of including anisotropy on the experimental performance of 3D topology-optimized beams manufactured by FFF. FFF is specifically chosen as the manufacturing process for this project as the anisotropy of the printed material is known to be high when using certain print machinery. During manufacture, infill in all solid regions is dictated to be along a certain direction for all layers, such that the anisotropic behavioral direction is known. This allows for an assumption of constant material behaviors along three main directions. Dog bone testing is performed to determine the material properties. Simply supported 3D beams are designed using topology optimization with both isotropic and anisotropic base material assumptions. Beam designs are obtained with different constraints on the material use, to investigate if anisotropy is more important to consider for certain design scenarios. The designs are printed using FFF in PLA and experimentally tested in 3-point bending.

This paper is organized as follows; first the used methodologies for design and experiments are outlined in Section 2. This includes the determination of the material properties of the used infill in Section 2.1, a description of the used topology optimization framework in Section 2.2, and the 3-bending test set-up in Section 2.3. Subsequently the obtained results are discussed in Section 3.

## 2. MATERIALS AND METHODS

This work consists of three main steps. The steps are as follows: (i) experimentally establishing material properties of the infill in two directions, (ii) using topology optimization to design with isotropic and anisotropic base materials and different allowable material volumes, and (iii) test the designs experimentally.

### 2.1 Experimental Determination of Material Properties

In this work all design are printed on a Prusa i3 MK3 desktop printer with 100% infill density and a nozzle diameter of 0.4mm. The material is commercial-grade polylactic acid (PLA) plastic, as distributed by Matterhackers [32]. Prior to obtaining the topology-optimized beam designs, the orientationally dependent Young's moduli are experimentally evaluated. The tests are conducted following the ASTM D638 Type 1 dog-bone tensile testing guidelines. The dimensions of the used dog-bones are shown in Fig. 2a. As it is herein assumed that the layer-by-layer anisotropy of the used printer is equivalent to the in-plane anisotropy, two different infill directions are considered; parallel (Fig. 2b) and perpendicular (Fig. 2c) to the main loading direction. Four specimens are tested for each infill direction.

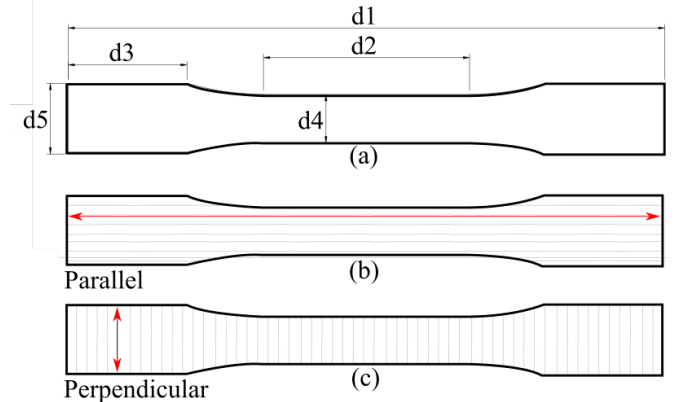


**FIGURE 2:** DOG-BONE TEST SPECIMENS TESTED ACCORDING TO ASTM D638 TYPE 1. (A) DOG-BONE SPECIMEN DIMENSIONS  $d_1 = 165.0$  mm,  $d_2 = 57.00$  mm,  $d_3 = 32.66$  mm,  $d_4 = 13.00$  mm,  $d_5 = 19.00$  mm. INFILL (B) (b) PARALLEL AND (C) PERPENDICULAR TO THE DIRECTION OF LOADING.

The tensile material tests are conducted on an Instron Universal Testing Machine as shown in Fig. 3. Extensometers are attached to the body of the dog-bone specimens to measure deformations. Tensile loads are applied at the top end while the specimens are clamped at the bottom. Three samples of each specimen type are tested till failure.

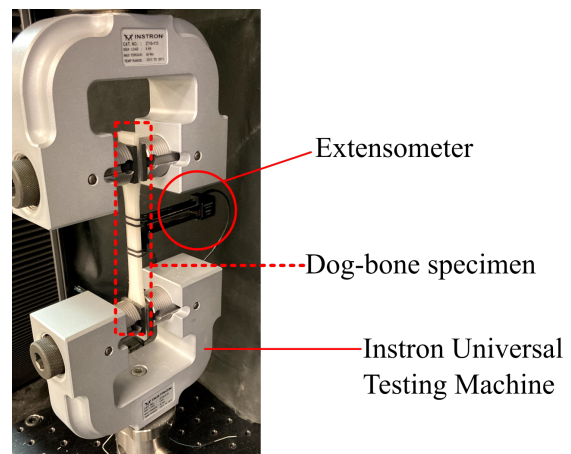


**FIGURE 3:** TENSILE TESTING SETUP. A DOG-BONE SPECIMEN IS CLAMPED AT THE TOP AND BOTTOM. AN EXTENSOMETER IS ATTACHED AT SPECIMEN CENTER TO MEASURE DISPLACEMENTS.

### 2.2 Topology Optimization

The design domain for the current work is defined as a 3D simply supported beam of length  $L = 135$  mm, height  $H = 45$  mm, and depth  $W = 18$  mm (see Fig. 4). The beam is supported by pins along the depth at one end and rollers along the depth at the opposite end. A load of total magnitude  $P = 2$  kN is distributed along the depth at mid-span. To save computation cost, symmetry is exploited to only design quarter of the design

space. The design domain is discretized using  $135 \times 90 \times 18$  linear brick elements.

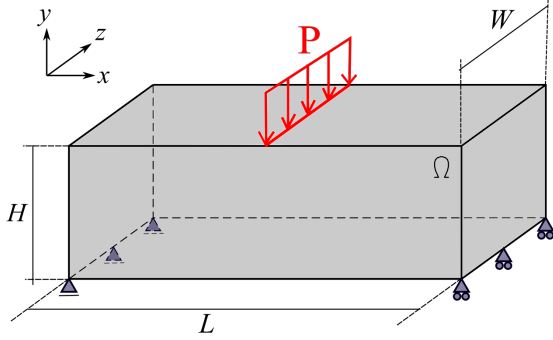


**FIGURE 4:** DESIGN DOMAIN FOR THE HEREIN CONSIDERED SIMPLY SUPPORTED BEAM PROBLEM. THE DIMENSIONS ARE TAKEN AS  $H = 45\text{mm}$ ,  $W = 18\text{mm}$ ,  $L = 135\text{mm}$ , AND  $P = 2\text{kN}$ .

The design problem is formulated as the classical compliance minimization problem subject to a material volume constraint. For a thorough introduction to the classical topology optimization compliance problem, solved using the density-based method, the reader is referred to [33]. The problem formulation used herein is as follows:

$$\begin{aligned} \min_{\rho_e^e} \quad & \mathbf{F}^T \mathbf{d} \\ \text{s. t.} \quad & \mathbf{K}(\rho) \mathbf{d} = \mathbf{F} \\ & \sum_{e \in \Omega} \rho_e^e v^e \leq V \\ & \rho_{min}^e \leq \rho^e \leq 1 \quad \forall e \in \Omega \end{aligned} \quad (1)$$

Here, the design variables are taken as the densities of the finite elements,  $\rho^e$ , within the design domain,  $\Omega$ . The objective function  $f$  is defined as the static compliance and is minimized with respect to a volume constraint  $g$ , while maintaining static equilibrium,  $h$ . The volume constraint is defined by a user determined desired volume,  $V$ , and is calculated by ensuring that the sum of the element density  $\rho^e$  of all the elements  $e$  in the design domain, times the element volume  $v^e$  does not exceed the desired volume. The static equilibrium constraint is defined as the global stiffness matrix,  $\mathbf{K}(\rho)$ , the nodal displacements,  $\mathbf{d}$ , and the global load vector,  $\mathbf{F}$ . Herein, linear-elastic behavior is assumed. As is outlined in Bendsoe and Sigmund's 2004 book [19], the design variables  $\rho^e$  are defined as continuous and bounded by  $\rho_{min}^e$  and 1. For this work,  $\rho_{min}^e$  is taken as 0.

To guide the design decisions towards a 0-1 solution, the Solid Isotropic Material Penalization (SIMP) method [34] is used to penalize intermediate densities:

$$\mathbf{K}_e(\rho^e) = (\rho_e^\eta + \rho_{min}) \mathbf{K}_0^e \quad (2)$$

The element stiffness matrix of a pure solid element is defined as  $\mathbf{K}_0^e$ , and  $\eta > 0$  is the exponent penalty term,  $\rho_{min}$  is a small positive number required to maintain positive definiteness

of the global stiffness matrix. Herein,  $\rho_{min}$  is taken as  $10^{-3}$ . Continuation is used on  $\eta$  which is taken from 1 to 3 in increments of  $\Delta\eta = 1$ .

This continuum topology optimization method requires filtering to avoid numerical instabilities when relating the design variables to the element densities. Herein, the Heaviside Projection Method is used as the filtering method [35]. Herein,  $r_{min}$  is taken as 1 mm and a constant Heaviside parameter of  $\beta = 50$  is used.

The optimization algorithm used to solve Eq. (1) is in this work the Method of Moving Asymptotes (MMA) [36].

### 2.3 Incorporation an Anisotropic Base Material

Since the prescribed infill in this work forces the anisotropic behavior to be in the same direction throughout the printed structures, the behavior of the bulk 3D printed material can be incorporated by modifying the element stiffness matrix of a purely solid element  $\mathbf{K}_0^e$ .

In classic finite element analysis, the element stiffness matrix is computed using the following equation:

$$\mathbf{K}_0^e = [\mathbf{B}^e]^T \mathbf{D} \mathbf{B}^e \quad (3)$$

Here  $\mathbf{B}^e$  is the strain displacement matrix and  $\mathbf{D}$  is constitutive matrix that describes the stress-strain behavior of the used material.

For isotropic materials, the following constitutive matrix is commonly used in 3D:

$$c_1 = \frac{E}{(1+\nu)(1-2\nu)} \quad (4)$$

$$\mathbf{D}_{iso} = c_1 \begin{bmatrix} 1-\nu & \nu & \nu & 0 & 0 & 0 \\ \nu & 1-\nu & \nu & 0 & 0 & 0 \\ \nu & \nu & 1-\nu & 0 & 0 & 0 \\ 0 & 0 & 0 & 1-2\nu & 0 & 0 \\ 0 & 0 & 0 & 0 & 1-2\nu & 0 \\ 0 & 0 & 0 & 0 & 0 & 1-2\nu \end{bmatrix} \quad (5)$$

For anisotropic materials, the constitutive matrix incorporates the  $x$ -,  $y$ -, and  $z$ -directions. It is convenient to define a coefficient  $c_2$  as:

$$c_2 = \frac{1-v_{xy}v_{yx}-v_{zy}v_{yz}-v_{xz}v_{zx}-2v_{xy}v_{yz}v_{zx}}{E_x E_y E_z} \quad (6)$$

For the purposes of this paper, the Poisson's ratio is taken as the same in all directions. It follows then that Eq. (6) can be simplified as follows:

$$c_2 = \frac{1-3\nu^2-2\nu^3}{E_x E_y E_z} \quad (7)$$

The constitutive matrix for an anisotropic base material is therefore taken as:

$$\mathbf{D}_{\text{ani}} = c_2 \begin{bmatrix} \frac{1-v^2}{E_y E_z c_2} & \frac{v+v^2}{E_y E_z c_2} & \frac{v+v^2}{E_y E_z c_2} & 0 & 0 & 0 \\ \frac{v+v^2}{E_x E_z c_2} & \frac{1-v^2}{E_x E_z c_2} & \frac{v+v^2}{E_x E_z c_2} & 0 & 0 & 0 \\ \frac{v+v^2}{E_y E_x c_2} & \frac{v+v^2}{E_y E_x c_2} & \frac{1-v^2}{E_y E_x c_2} & 0 & 0 & 0 \\ 0 & 0 & 0 & G_{yz} & 0 & 0 \\ 0 & 0 & 0 & 0 & G_{zx} & 0 \\ 0 & 0 & 0 & 0 & 0 & G_{xy} \end{bmatrix} \quad (8)$$

For computationally derived results, the isotropic constitutive matrix is used for the isotropic models while the anisotropic constitutive matrix is used for the anisotropic models.

## 2.4 Experimental Evaluation of Designs

The beam specimens are printed on the same printing setup as the dog-bone tests (Prusa i3 MK3 desktop printer using PLA plastic material). The specimens are tested using a 3-point bending test according to ASTM D790 guidelines on an Instron Universal Testing Machine (See Fig. 5). The Instron Testing Machine simultaneously records both the displacement and the applied force until failure. The measurements are taken from the center of the specimen. For each specimen type a total of 3 samples are fabricated and tested. To prevent the specimens from slipping out of the testing apparatus, the supports were offset by 5mm on each side. It should be noted that this was not accounted for in the design problem formulation.

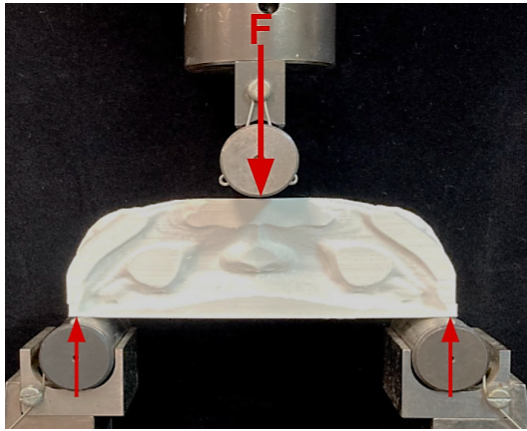


**FIGURE 5:** THREE POINT BENDING TEST SETUP. NOTE THAT THE SUPPORTS HAVE BEEN MOVED 5MM IN ON EACH SIDE.

## 3. RESULTS AND DISCUSSION

### 3.1 Experimental Investigation of Material Behavior

The results from the tensile tests of the dog-bone specimens are listed in Tab. 1 and Figure 6. It is clearly seen that there is a non-negligible directional difference in performance. The used PLA filament has a published Young's Modulus of 3.60 GPa [32]. With the specific infill and printing method chosen, the closest the AM material gets to achieving the published design value is, at best, 89% (3.22 GPa).

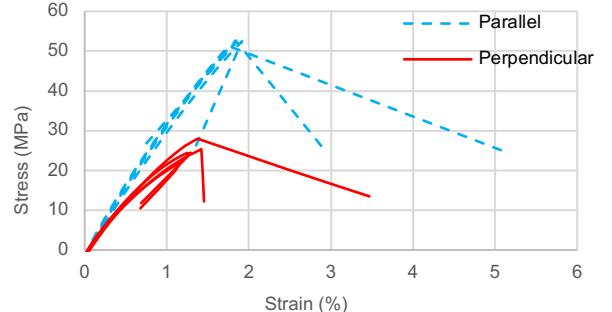


**FIGURE 6:** STRESS VS. STRAIN CURVES OF PARALLEL (DOTTED) AND PERPENDICULAR (SOLID) DOG-BONE SPECIMENS

**TABLE 1:** YOUNG'S MODULUS VALUES OBTAINED FOR DOG-BONE TENSILE TESTING WITH INFILL IN TWO DIFFERENT DIRECTIONS.

Sample No.	Young's Modulus (GPa)	
	Parallel	Perpendicular
1	3.20	2.32
2	3.12	2.26
3	2.95	2.49
4	3.22	2.29
<b>Average</b>	<b>3.12</b>	<b>2.34</b>

As expected, there is also a significant difference between the parallel and perpendicular infill directions. In this work, a 28.6% difference in the average Young's Modulus is observed between the two infill directions.

In the design conducted herein, the  $x$ -direction of the design domain (along the span length of the beam) is chosen to have the stiffest material direction. This is enforced by fabricating all designs using horizontally parallel infill. The following equation is therefore used to relate the Young's Modulus values in  $x$ ,  $y$  and  $z$ :

$$E_y = E_z = (1 - 0.286)E_x \quad (9)$$

### 3.2 Topology-Optimized Designs

The 3D beam design results are obtained by solving Eq. (1) with volume constraints of 25%, 50%, 75%. As mentioned, both isotropic and anisotropic base material assumptions are used for the designs. For isotropic designs, the Young's modulus is taken as  $E = 3.12$  GPa, whereas for the anisotropic designs  $E_x = 3.12$  GPa is used only for the  $x$ -direction. In  $y$ - and  $z$ -directions, the base material stiffness is defined by  $E_y = E_z = 2.34$  GPa. All designs use a constant Poisson's ratio of  $\nu = 0.3$ .

The obtained designs are shown in Figs 7 and 8. Given the parameters used, the resultant designs fall in-line with the generalizations of the optimization technique [37]. Namely, that smaller  $r_{min}$  values result in more shell-like structures while larger  $r_{min}$  values result in more holes.

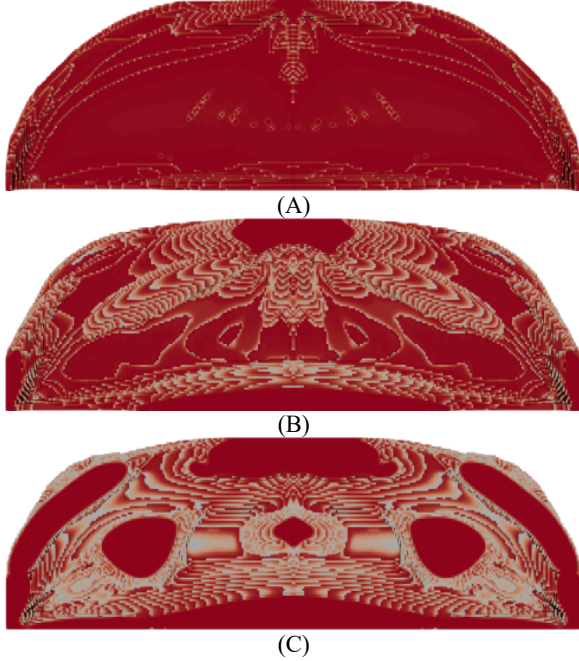


**FIGURE 7:** ANISOTROPIC TOPOLOGY-OPTIMIZED DESIGN RESULTS WITH MATERIAL RESTRICTIONS OF (A) 25%, (B) 50%, AND (C) 75%.

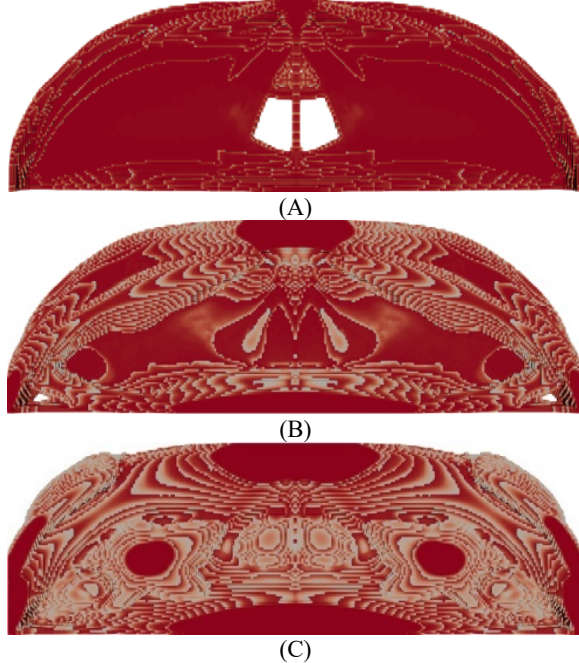


**FIGURE 8:** ISOTROPIC TOPOLOGY-OPTIMIZED DESIGN RESULTS WITH MATERIAL RESTRICTIONS OF (A) 25%, (B) 50%, AND (C) 75%.

Some notable features of the designs are that the lower volume fraction isotropic designs (See Fig. 8A, Fig. 8B) have holes in the design that penetrate through the entire specimen. These holes subsequently effect fabricability because they require support structures. In contrast, no penetrating holes appear in the anisotropic solutions (Fig. 7). All obtained designs in Fig.s 7 and 8 have outer contours that resemble thin flanges along the beam bottom and the top arch. However, these flanges are observed to be thicker for the anisotropic designs, to accommodate the directional properties of the base material.

The computational designs are processed in the Cura Slicer Engine before being sent to the 3D printer. As can be seen in the Cura Slicer Engine example shown in Fig. 9, the infill is forced to be 100% density, and only go in the  $x$ -direction. A support structure is only required for the 25% isotropic design.

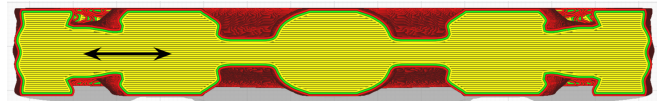


**FIGURE 9:** 75% ANISOTROPIC SPECIMEN PLACED IN CURA SLICER ENGINE. ARROW INDICATES THE DIRECTION OF INFILL.

Figure 10 shows examples of the printed beam specimens. Three specimens are fabricated of each type. In addition to the topology-optimized designs, a 100% volume specimen is fabricated and tested (Fig. 10G). It has material that fills the entire design domain of 135mm x 45mm x 18mm. Cubic additions to the ends of the 25% designs were added to ensure that there will be enough surface area touches the supports in testing. Visually, the computational designs align well with the fabricated specimens. There is some evidence of surface texture that is non-existent in the generated computational designs, but this can be explained by the incomplete removal of support structures and due to minor amounts of overhang resulting in minor amounts of drippage. The only post-processing of the specimens is the manual removal of support structures.

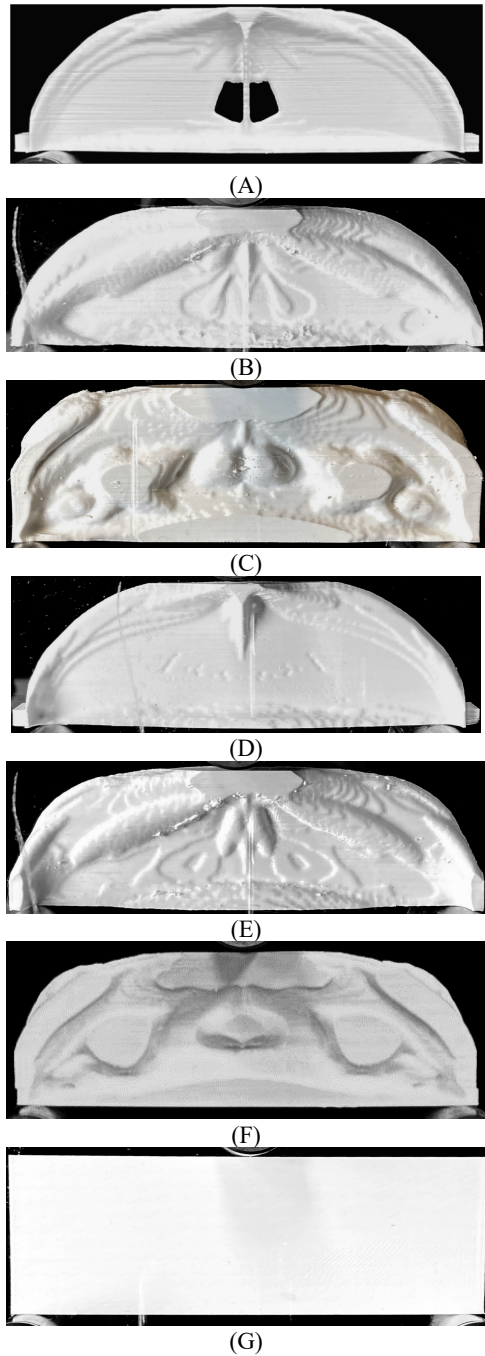


**FIGURE 10:** PRINTED BEAM SPECIMENS WITH MATERIAL RESTRICTIONS OF (A, D) 25%, (B, E) 50%, (C, F) 75%, AND (G) 100%. ISOTROPIC MATERIAL ASSUMPTIONS ARE USED TO OBTAIN (A, B, C), WHEREAS (D, E, F) ARE OBTAINED WITH ANISOTROPIC ASSUMPTIONS.

At and below 50% volume fraction, the isotropic designs become difficult to fabricate. The 50% isotropic design has small but clear internal holes near the supports (see Fig. 7B), but these holes are evident in the fabricated specimens (See Fig. 10C). At 25% volume fraction, the isotropic design becomes very difficult to fabricate using a the herein considered FFF process. The large

amounts of overhang and extremely slender members within the design results in a successful fabrication rate of 33.33%.

Figure 11 shows images of problems encountered with printing of the isotropic designs. In Fig. 11A-B, a print failure in the thin struts is documented for a 25% isotropic design. Fig 11C shows how the increased level of overhang in the 75% isotropic design results in a high level of surface imperfections. In contrast, the anisotropic designs have a 100% success rate with default print settings and no support material.

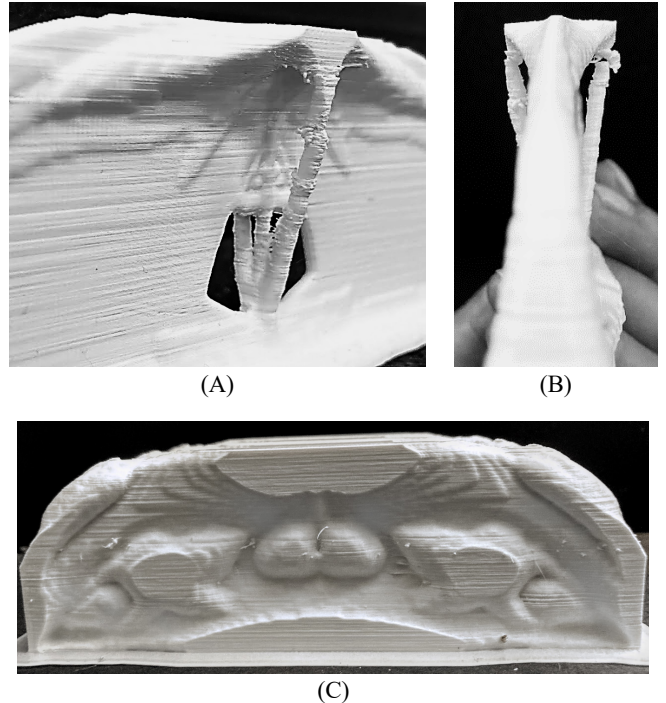


**FIGURE 11:** FABRICATION ERRORS AND IMPERFECTIONS: (A-B) THIN STRUTS OF 25% ISOTROPIC SPECIMENS ARE DIFFICULT TO REALIZE, AND (C) NOTICABLE SURFACE IMPERFECTIONS ARE PRESENT IN 75% ISOTROPIC SPECIMENS DUE TO SIGNIFICANT PRESENCE OF OVERHANGING FEATURES.

### 3.3 Experimental Beam Behavior

Figure 12 shows the experimentally obtained force versus displacement plots for all the printed beam specimens. Not surprisingly, as the material volume increases, so too does the stiffness and strength of the specimens. There is a marginal improvement in stiffness performance in the anisotropic specimens over the isotropic specimens with the same material volume. However, there is also a larger spread in performance of the isotropic specimens.

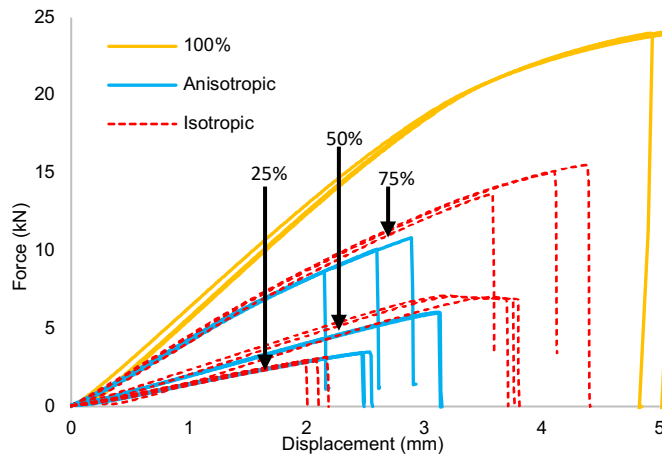


**FIGURE 12:** FORCE VS. DISPLACEMENT RELATIONS OBTAINED FOR ALL TESTED SPECIMENS. ALL SPECIMENS ARE SEEN TO EXHIBIT LINEAR ELASTIC BEHAVIOR AT THE 2 kN DESIGN LOAD.

The behavior of the 75% volume fraction designs exhibited significant variation across both isotropic and anisotropic designs. It is noted that these specimens exhibited explosive failure due to the high density, and it is stipulated to be due to internal defects of the fabricated specimen. For more concrete justification of why these designs did not behave consistently, further investigation is required.

All design in this work were obtained for a design load of  $P = 2$  kN, under the assumption of linear elastic behavior. In Fig. 12 it is seen that linear force-displacement behavior is present for all samples at  $P = 2$  kN and thus that the assumption here holds for all tested designs. Tab. 2 compares the numerical and experimental behaviors at the design load. It shows the average experimental performance and the computed performance value of each specimen at the design load. It is notable that the numerical results are consistently significantly greater than the experimentally observed performance. This can be explained by the fact that the boundary conditions in testing differ slightly from in the computational models as they are moved 5 mm inward on each side.

**TABLE 2:** AVERAGE COMPUTED AND EXPERIMENTAL COMPLIANCE VALUES OF 3D BEAM SPECIMENS

Volume	Material	Compliance (kNm)	
		Computed	Experimental
25%	<i>isotropic</i>	4.25	2.69
	<i>anisotropic</i>	3.97	2.74
50%	<i>isotropic</i>	2.35	2.02
	<i>anisotropic</i>	2.37	2.03
75%	<i>isotropic</i>	1.85	0.97
	<i>anisotropic</i>	1.77	0.99
100%	<i>isotropic</i>	1.50	0.86
	<i>anisotropic</i>	1.51	-

This suggests that the accuracy of the boundary conditions plays a significant factor in determining the accuracy of the performance.

When comparing the experimental performance values in Fig. 13, it is seen that there is not a notable difference between average performance of the isotropic and the anisotropic designs (1.8-2.0%). However, the isotropic designs have a larger standard deviation for all material volumes.

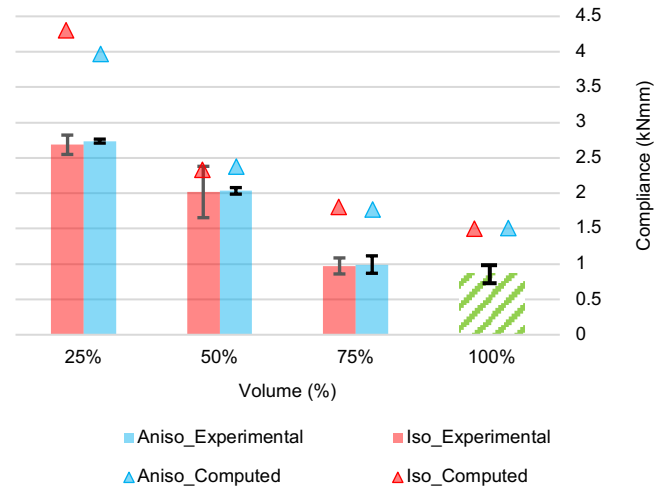


**FIGURE 13:** EXPERIMENTAL COMPLIANCE VALUES WITH STANDARD DEVIATION AND NUMERICAL COMPLIANCE VALUES (TRIANGLES) SUPERIMPOSED. ISOTROPIC DESIGNS (RED), AND ANISOTROPIC DESIGNS(BLUE).

To more clearly illustrate this, Fig. 14 gives the average compliance and standard deviation values at the design load. As expected, Fig. 14A shows no notable difference between the average performance of the isotropic versus the anisotropic designs. In contrast, Figure 14B indicates that there is a definite improvement in the consistency of the performance of the anisotropic designs.

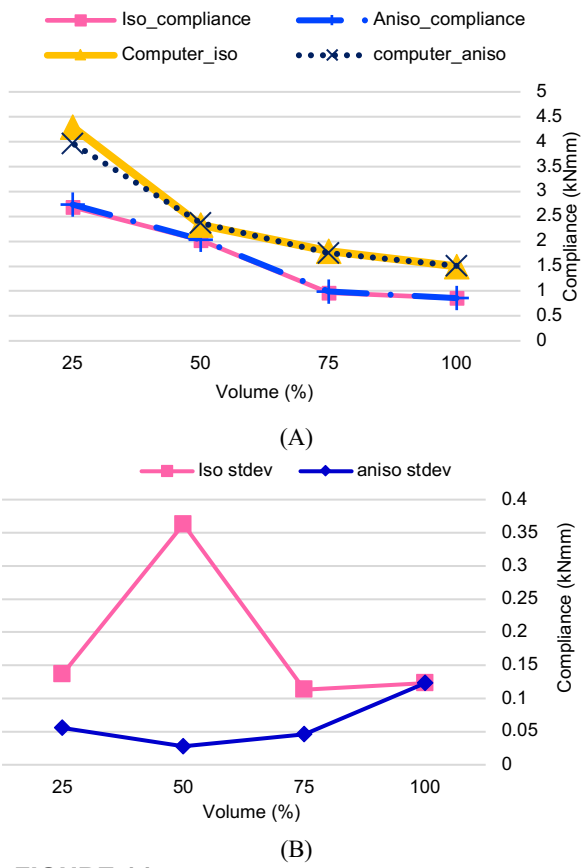


**FIGURE 14:** AVERAGE (A) COMPLIANCE AND (B) STANDARD DEVIATION.

The anisotropic beam tests varied from 0.03–0.06 kNm over the herein considered material volumes. In comparison, the observed standard deviation for the isotropic specimens was in the range 0.11–0.39 kNm. The standard deviation is thus 84.4 – 171.5% higher for the isotropic designs than for their anisotropic counterparts. This large discrepancy comes in addition to the fact that a greater number of isotropic specimens had to be printed to conduct three tests at each material volume (the success rate was e.g. only 33% for the 25% isotropic design).

#### 4. CONCLUSION

This work has conducted an experimental investigation to examine the effects of including anisotropic material assumptions in a topology optimization design framework. All specimens have been fabricated using FFF as this has allowed us to prescribe the infill and thus anisotropy in a specified direction along the design domain. Prior to obtaining the designs, the directional variation of the material behavior was determined through dog-bone tests.

Topology-optimized simply supported 3D beams were designed with material volumes of 25%, 50%, 75%, and compared to a 100% beam. Designs were obtained with both isotropic and anisotropic base materials. While all anisotropic designs were easily manufacturable, fabrication of the isotropic specimens at and below 50% volume was more difficult. The rate

of successful fabrication of the 25% isotropic design was only 33.3%. Upon successful fabrication of three specimens of each type, all beams were tested till failure.

The results of the experimental analysis indicate that including anisotropy alone does not significantly alter the average behavior at the design load for the herein considered design case. Worth noting is, however, that the anisotropic beam specimens exhibited a more uniform behavior across samples compared to the isotropic beams with the same volume. This study therefore suggests that inclusion of anisotropy within topology optimization frameworks does not affect the average design performance. However, it does limit variation in performance of fabricated specimens and may implicitly improve the design manufacturability and reliability.

#### REFERENCES

- [1] A. W. Ganczarski, H. Egner, and J. J. Skrzypek, “Introduction to Mechanics of Anisotropic Materials,” in *Mechanics of Anisotropic Materials*, J. J. Skrzypek and A. W. Ganczarski, Eds. Cham: Springer International Publishing, 2015, pp. 1–56. doi: 10.1007/978-3-319-17160-9\_1.
- [2] U. M. Dilberoglu, B. Gharehpapagh, U. Yaman, and M. Dolen, “The Role of Additive Manufacturing in the Era of Industry 4.0,” *Procedia Manufacturing*, vol. 11, pp. 545–554, Jan. 2017, doi: 10.1016/j.promfg.2017.07.148.
- [3] F. Bos, R. Wolfs, Z. Ahmed, and T. Salet, “Additive manufacturing of concrete in construction: potentials and challenges of 3D concrete printing,” *Virtual and Physical Prototyping*, vol. 11, no. 3, pp. 209–225, Jul. 2016, doi: 10.1080/17452759.2016.1209867.
- [4] P. Wu, J. Wang, and X. Wang, “A critical review of the use of 3-D printing in the construction industry,” *Automation in Construction*, vol. 68, pp. 21–31, Aug. 2016, doi: 10.1016/j.autcon.2016.04.005.
- [5] “Additive Manufacturing - ASTM International.” <https://www.astm.org/industry/additive-manufacturing-overview.html> (accessed Jul. 09, 2021).
- [6] K. V. Wong and A. Hernandez, “A Review of Additive Manufacturing,” *ISRN Mechanical Engineering*, vol. 2012, pp. 1–10, Aug. 2012, doi: 10.5402/2012/208760.
- [7] P. Zhang, J. Liu, and A. C. To, “Role of anisotropic properties on topology optimization of additive manufactured load bearing structures,” *Scripta Materialia*, vol. 135, pp. 148–152, Jul. 2017, doi: 10.1016/j.scriptamat.2016.10.021.
- [8] N. Guo and M. C. Leu, “Additive manufacturing: technology, applications and research needs,” *Front. Mech. Eng.*, vol. 8, no. 3, pp. 215–243, Sep. 2013, doi: 10.1007/s11465-013-0248-8.
- [9] M. Fernandez-Vicente, W. Calle, S. Ferrandiz, and A. Conejero, “Effect of Infill Parameters on Tensile Mechanical Behavior in Desktop 3D Printing,” *3D Printing and Additive Manufacturing*, vol. 3, no. 3, pp. 183–192, Sep. 2016, doi: 10.1089/3dp.2015.0036.

- [10] P. Zhang and A. C. To, "Transversely isotropic hyperelastic-viscoplastic model for glassy polymers with application to additive manufactured photopolymers," *International Journal of Plasticity*, vol. 80, pp. 56–74, May 2016, doi: 10.1016/j.ijplas.2015.12.012.
- [11] A. Cazón, P. Morer, and L. Matey, "PolyJet technology for product prototyping: Tensile strength and surface roughness properties," *Proceedings of the Institution of Mechanical Engineers, Part B: Journal of Engineering Manufacture*, vol. 228, no. 12, pp. 1664–1675, Dec. 2014, doi: 10.1177/0954405413518515.
- [12] S. Ahn, M. Montero, D. Odell, S. Roundy, and P. K. Wright, "Anisotropic material properties of fused deposition modeling ABS," *Rapid Prototyping Journal*, vol. 8, no. 4, pp. 248–257, Jan. 2002, doi: 10.1108/13552540210441166.
- [13] A. Bellini and S. Güceri, "Mechanical characterization of parts fabricated using fused deposition modeling," *Rapid Prototyping Journal*, vol. 9, no. 4, pp. 252–264, Jan. 2003, doi: 10.1108/13552540310489631.
- [14] A. R. Torrado and D. A. Roberson, "Failure Analysis and Anisotropy Evaluation of 3D-Printed Tensile Test Specimens of Different Geometries and Print Raster Patterns," *J Fail. Anal. and Preven.*, vol. 16, no. 1, pp. 154–164, Feb. 2016, doi: 10.1007/s11668-016-0067-4.
- [15] N. G. Tanikella, B. Wittbrodt, and J. M. Pearce, "Tensile strength of commercial polymer materials for fused filament fabrication 3D printing," *Additive Manufacturing*, vol. 15, pp. 40–47, May 2017, doi: 10.1016/j.addma.2017.03.005.
- [16] C. S. Lee, S. G. Kim, H. J. Kim, and S. H. Ahn, "Measurement of anisotropic compressive strength of rapid prototyping parts," *Journal of Materials Processing Technology*, vol. 187–188, pp. 627–630, Jun. 2007, doi: 10.1016/j.jmatprotec.2006.11.095.
- [17] M. K. Thompson *et al.*, "Design for additive manufacturing: trends, opportunities, considerations, and constraints," Jun. 2016, doi: 10.1016/j.cirp.2016.05.004].
- [18] Z. Doubrovski, J. C. Verlinden, and J. M. P. Geraedts, "Optimal Design for Additive Manufacturing: Opportunities and Challenges," Jun. 2012, pp. 635–646, doi: 10.1115/DETC2011-48131.
- [19] M. P. Bendsoe and O. Sigmund, *Topology Optimization: Theory, Methods, and Applications*, 2nd ed. Springer-Verlag: Berlin Germany, 2004.
- [20] O. Sigmund and K. Maute, "Topology optimization approaches," *Struct Multidisc Optim*, vol. 48, no. 6, pp. 1031–1055, Dec. 2013, doi: 10.1007/s00158-013-0978-6.
- [21] O. Sigmund, "On the usefulness of non-gradient approaches in topology optimization," *Struct Multidisc Optim*, vol. 43, no. 5, pp. 589–596, May 2011, doi: 10.1007/s00158-011-0638-7.
- [22] M. P. Bendsøe, "Optimal shape design as a material distribution problem," *Structural Optimization*, vol. 1, no. 4, pp. 193–202, Dec. 1989, doi: 10.1007/BF01650949.
- [23] J. Liu *et al.*, "Current and future trends in topology optimization for additive manufacturing," *Struct Multidisc Optim*, vol. 57, no. 6, pp. 2457–2483, Jun. 2018, doi: 10.1007/s00158-018-1994-3.
- [24] C. Dapogny, R. Estevez, A. Faure, and G. Michailidis, "Shape and topology optimization considering anisotropic features induced by additive manufacturing processes," *Computer Methods in Applied Mechanics and Engineering*, vol. 344, pp. 626–665, Feb. 2019, doi: 10.1016/j.cma.2018.09.036.
- [25] J. V. Carstensen, "Topology optimization with nozzle size restrictions for material extrusion-type additive manufacturing," *Struct Multidisc Optim*, vol. 62, no. 5, pp. 2481–2497, Nov. 2020, doi: 10.1007/s00158-020-02620-5.
- [26] R. Hoglund and D. E. Smith, "Continuous Fiber Angle Topology Optimization for Polymer Fused Filament Fabrication," 2016. Accessed: Feb. 09, 2022. [Online]. Available: <https://repositories.lib.utexas.edu/handle/2152/89657>
- [27] D. R. Jantos, K. Hackl, and P. Junker, "Topology optimization with anisotropic materials, including a filter to smooth fiber pathways," *Struct Multidisc Optim*, vol. 61, no. 5, pp. 2135–2154, May 2020, doi: 10.1007/s00158-019-02461-x.
- [28] D. Jiang, R. Hoglund, and D. Smith, "Continuous Fiber Angle Topology Optimization for Polymer Composite Deposition Additive Manufacturing Applications," *Fibers*, vol. 7, p. 14, Feb. 2019, doi: 10.3390/fib7020014.
- [29] E. Ulu, E. Korkmaz, K. Yay, O. Burak Ozdoganlar, and L. Burak Kara, "Enhancing the Structural Performance of Additively Manufactured Objects Through Build Orientation Optimization," *Journal of Mechanical Design*, vol. 137, no. 11, Oct. 2015, doi: 10.1115/1.4030998.
- [30] N. Umetani and R. Schmidt, "Cross-sectional structural analysis for 3D printing optimization," in *SIGGRAPH Asia 2013 Technical Briefs*, New York, NY, USA, Nov. 2013, pp. 1–4. doi: 10.1145/2542355.2542361.
- [31] A. M. Mirzendehdel, B. Rankouhi, and K. Suresh, "Strength-based topology optimization for anisotropic parts," *Additive Manufacturing*, vol. 19, pp. 104–113, Jan. 2018, doi: 10.1016/j.addma.2017.11.007.
- [32] MatterHackers inc., "Technical Data Sheet – Build Series PLA," 2021, [Online]. Available: <https://www.matterhackers.com/store/l/175mm-pla-filament-black-1-kg/sk/MY6CYEZM>.
- [33] O. Sigmund, "A 99 line topology optimization code written in Matlab," *Struct Multidisc Optim*, vol. 21, no. 2, pp. 120–127, Apr. 2001, doi: 10.1007/s001580050176.
- [34] M. P. Bendsøe and O. Sigmund, "Material interpolation schemes in topology optimization," *Archive of Applied Mechanics*, vol. 69, no. 9, pp. 635–654, Nov. 1999, doi: 10.1007/s004190050248.
- [35] J. K. Guest, J. H. Prévost, and T. Belytschko, "Achieving minimum length scale in topology optimization using nodal design variables and projection functions," *International Journal for Numerical Methods in Engineering*, vol. 61, no. 2, pp. 238–254, 2004, doi: 10.1002/nme.1064.

- [36] K. Svanberg, “The method of moving asymptotes—a new method for structural optimization,” *International Journal for Numerical Methods in Engineering*, vol. 24, no. 2, pp. 359–373, 1987, doi: 10.1002/nme.1620240207.
- [37] O. Sigmund, N. Aage, and E. Andreassen, “On the (non-)optimality of Michell structures,” *Struct Multidisc Optim*, vol. 54, no. 2, pp. 361–373, Aug. 2016, doi: 10.1007/s00158-016-1420-7.